Magnetism-induced symmetry breaking in photoelectron diffraction patterns

A. Chassé
Physics Department, Martin-Luther-University Halle-Wittenberg, D-06099 Halle, Germany

W. Kuch*
Max-Planck-Institut für Mikrostrukturphysik, Weinberg 2, D-06120 Halle, Germany

M. Kotsugi†
Graduate School of Engineering Science, Osaka University, 1-3 Machikaneyama, Toyonaka 560-8531, Japan

Xingyu Gao‡ and F. Offi§
Max-Planck-Institut für Mikrostrukturphysik, Weinberg 2, D-06120 Halle, Germany

S. Imada and S. Suga
Graduate School of Engineering Science, Osaka University, 1-3 Machikaneyama, Toyonaka 560-8531, Japan

H. Daimon
Graduate School of Materials Science, Nara Institute of Science and Technology, Ikoma, Nara 630-0192, Japan and CREST-JST, 4-1-8 Honcho, Kawaguchi, Saitama, Japan

J. Kirschner
Max-Planck-Institut für Mikrostrukturphysik, Weinberg 2, D-06120 Halle, Germany
(Received 24 September 2003; revised manuscript received 9 September 2004; published 31 January 2005)

The magnetism-induced symmetry breaking in photoelectron diffraction patterns of $2p_{3/2}$ photoelectrons from a ferromagnetic Fe(001) single crystal surface is studied experimentally and theoretically. Two-dimensional photoelectron intensity angular distribution patterns were recorded at 1193 eV photon energy for both helicities of the circularly polarized light and for opposite magnetization directions of the sample by a display-type spherical mirror analyzer, which allows simultaneous energy and momentum analysis of emitted photoelectrons. The macroscopic magnetization of the sample induces an additional symmetry breaking in the circular dichroism of the Fe $2p_{3/2}$ photoelectron angular distribution patterns which is related to the presence of magnetic moments on the Fe atoms. Multiple-scattering cluster photoelectron diffraction calculations agree well with experiment, and reproduce even fine details of the observed photoelectron diffraction features. The details of that breaking of mirror symmetry of photoelectron scattering in the plane spanned by light incidence and electron emission due to the presence of a magnetization within that plane depends both on the structure and the magnetism of the sample. In connection with multiple scattering calculations, measurements of the magnetism-induced symmetry breaking by two-dimensional photoelectron diffraction patterns may thus be used as a powerful tool for simultaneous structural and magnetic investigations of single crystalline magnetic samples and ultrathin films.

DOI: 10.1103/PhysRevB.71.014444 PACS number(s): 79.60.Bm, 75.25.+z, 71.20.Be, 71.70.Ej

I. INTRODUCTION

Photoelectron diffraction (PED) is a well-established technique in surface science for probing the local structure in a solid. When a photoelectron is emitted from a core level of an atom, its wave field interferes coherently with components elastically scattered by the surrounding atoms. This leads to variations in the measured photoelectron flux as a function of emission angle and energy. These diffraction effects contain information about the local crystal structure in the vicinity of the emitting atom. In single crystalline systems this can be used to determine the structure at surfaces, adsorbates, or thin films.[1]

The intensity of photoelectrons emitted under certain angles from magnetic samples exhibits a characteristic dependence on the magnetization direction. This is termed magnetic dichroism in the angular distribution (MDAD) of photoelectrons. It occurs for various experimental geometries, involving circularly,[2–4] linearly,[4–6] or even unpolarized light,[7–12] and can be observed in valence band[2,6,7,13] or core level photoemission spectra.[3–5,8–12]

It seems obvious that the combination of PED and magnetic dichroism of photoelectrons from core levels should allow one to study structural and magnetic properties of a surface or thin film at the same time, even with elemental resolution. On the one hand the appearance of magnetic dichroism in core-level photoemission from closed shells is related to the interaction of spin-orbit and intra-atomic exchange coupling, where the last one connects closed-shell spins with the magnetically ordered spins of the open shell.[14,15] On the other hand the dependence of the photoelectron intensity in angle-resolved photoemission on the

wave vector **k** is strongly modulated by photoelectron diffraction effects which are related to the local structural order in the sample. It has been shown that appropriate theoretical modeling of multiple scattering of photoelectrons plays an essential role in the interpretation of magnetic dichroism measurements using angle-resolved core-level photoemission. First quantitative explanations of MDAD of photoelectrons from core levels have been obtained by means of relativistic multiple-scattering formalism treating the final state as bulklike[14] and as a time-reversed low-energy electron diffraction (LEED) state.[16] Furthermore photoelectron diffraction by itself emerges as an important new source of magnetic dichroism in core-level photoelectron emission as shown for linearly,[9] circularly,[17] and unpolarized light.[11]

Additional information is expected if the effect of the spin of the electrons on the scattering is considered, which has been done for circularly polarized[17] and unpolarized light.[18] The influence of spin-dependent electron scattering on MDAD has been studied for geometries in which the angle between light incidence and electron emission was kept constant, while the crystal lattice was rotated.[9,11,19] Strong effects of the relative spin direction on the photoelectron intensity along forward scattering directions were found, which bear the potential for extracting structurally selective magnetic information, or magnetically selective structural information.[10]

In this paper we investigate the full two-dimensional angular dependence of photoelectrons emitted from a magnetic sample by circularly polarized light to get information about the local magnetic and structural order in the sample at the same time. Different from a former theoretical work[20] we focus on higher kinetic energy of several hundred eV, for which the intensity of photoelectrons is focused along forward scattering directions from the emitter atom along chains of neighboring scattering atoms. If circularly polarized x rays are used to excite photoelectrons with several hundred eV, the angular positions of the expected intensity maxima due to photoelectron diffraction are moved in a way which has been described as "peak rotation" in the angular distribution of photoelectrons.[21,22] Depending on the helicity of the exciting x rays, the forward focusing photoelectron diffraction maxima are rotated azimuthally clockwise or anticlockwise about the light incidence direction. The influence of a certain magnetic order in the vicinity of the emitting atom on such a two-dimensional photoelectron angular distribution has been already studied theoretically, and had been described by an additional "symmetry breaking" due to the presence of a macroscopic magnetization.[23–25] Magnetization-dependent differences in the details of the "peak rotation", which lead to this loss of symmetry, contain structural and magnetic information about the scattering atoms.[25]

We present here a combined theoretical and experimental study of magnetic effects on the circular dichroism in the angular distribution of photoelectrons from a magnetic Fe(001) surface. Full two-dimensional PED patterns were recorded for fixed electron energy to manifest the symmetry breaking by the sample magnetization experimentally. The advantage of this approach is that differences in the symmetry of the local structure around the emitting atoms become directly visible in the recorded patterns. We have found that the presence of magnetism in Fe(001) leads to sizeable symmetry breaking effects of about 10%. While the main effect is a different overall photoelectron intensity, also the angular positions and relative strength of the forward focusing photoelectron diffraction maxima are found to be influenced by the magnetism of the sample. From the comparison of experimental and calculated patterns, the influence of both the magnetic order and the geometric order in the sample can thus be studied in detail.

For the treatment of local effects the final state of photoelectrons is calculated within a multiple-scattering cluster (MSC) model where both spin–orbit and exchange interaction are included simultaneously. Whereas a slab method[26] requires the assumption of full translational symmetry parallel to the surface, a cluster-based theory is inherently more suitable for PED modeling in view of the point source nature of the problem and the sensitivity to short-range rather than long-range order. In this way the model allows one to associate certain structures in the diffraction patterns with the local structure around the emitting atom. We find that MSC calculations can well describe the experimental observations. The excellent agreement between experiment and theory with respect to the angular distribution of the magnetism-induced modifications of the photoelectron diffraction intensity indicate that detailed MSC calculations in combination with measurements of magnetic dichroism in photoelectron diffraction patterns bear the potential for the study of structural and magnetic properties of magnetic single crystalline systems.

The organization of the paper is as follows: In Sec. II the experimental details are presented. The display-type spherical mirror analyzer is described, which has been applied for recording 2π-photoelectron diffraction patterns. We briefly introduce in Sec. III the theory of photoelectron diffraction within a multiple-scattering cluster model. It includes both the spin–orbit and exchange interactions in the initial state. Experimental and theoretical results of the magnetism-induced symmetry breaking in the photoelectron angular distribution patterns are presented and discussed in Sec. IV. A short summary and outlook will be given in Sec. V.

II. EXPERIMENT

The experiments were performed at room temperature in an ultrahigh vacuum chamber with a base pressure of 2×10^{-8} Pa. The sample was a 0.8 mm wide and $\approx$10 mm long Fe(001) whisker.[27] Its surface was prepared by repeated cycles of 1.5 keV Ar^+ sputtering at 570 K, followed by a 2 min anneal to 900 K. Low-energy electron diffraction (LEED) showed a sharp (1×1) diffraction pattern, although Auger electron spectroscopy revealed the presence of small traces of carbon contamination after cooling the sample to room temperature.

Circularly polarized synchrotron radiation from the twin helical undulator beamline BL25SU of SPring-8 in Japan was used.[28] Light emitted in the first harmonic by one of the two undulators with a degree of circular polarization of about 98% at the sample position was used. Helicity reversal was

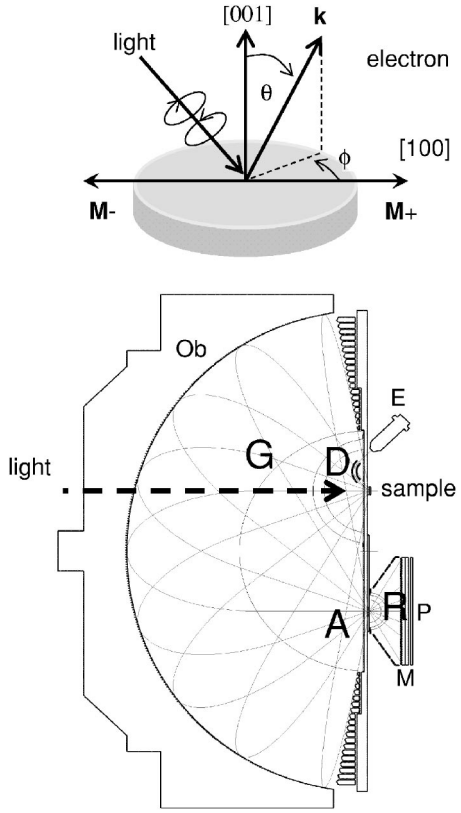

FIG. 1. (a) Sketch of the experimental geometry. Light is incident to the sample under an angle of 45° with respect to surface normal, along the [100] azimuth. The sample magnetization was switched between [100] (M^+) and $[\bar{1}00]$ (M^-). Electron emission directions are characterized by polar angle θ and azimuthal angle ϕ. (b) Schematic drawing of the display-type spherical mirror analyzer. *G*: hemispherical grids, *Ob*: obstacle rings, *A*: exit aperture, *R*: retardation grids, *M*: microchannel plate, *P*: phosphorous screen, *E*: electron gun, and *D*: deflector.

realized by switching between the two undulators after having set them to opposite helicity, i.e., by closing one undulator and fully opening the other. The entrance and exit slits of the monochromator were set to 45 and 200 μm, respectively, corresponding to a photon energy resolution of ≈1.6 eV. In order to limit the size of the light spot at the sample position, an aperture of 0.5 mm diameter was inserted between the exit slit and the refocusing mirror. This resulted in a spot size of 0.2 mm diameter on the sample. A sketch of the experimental geometry is presented in Fig. 1(a). The x rays were incident to the sample under an angle of 45° with respect to surface normal, along the long axis of the whisker, i.e., along the [100] azimuth of the sample. The magnetization of the sample was either along [100] (called $\boldsymbol{M}^+$ in the following) or along $[\bar{1}00]$ ($\boldsymbol{M}^-$). Photoelectrons were collected within a cone of $\theta < 60°$ from the surface normal ([001]). The direction of electron wave vector $\boldsymbol{k}$ is characterized by the polar angle θ and azimuthal angle ϕ, as defined in Fig. 1(a).

Photoelectrons were collected as two-dimensional photoelectron intensity angular distribution patterns by a display-type spherical mirror analyzer, which allows simultaneous energy and momentum analysis of the emitted photoelectrons.[29] A scheme of the setup is shown in Fig. 1(b). Here the [100] direction is pointing out of the drawing plane. The light is thus incident under 45° from behind the drawing plane, along the direction indicated by the dashed arrow. Electrons leaving the sample are directed to the exit aperture *A* by electrostatic fields created by hemispherical grids *G* and obstacle rings *Ob*. Energy resolution is achieved by the obstacle rings acting as a low-pass energy filter and retardation grids *R* behind the exit aperture as the corresponding high-pass filter. The energy-filtered electrons are intensified by a pair of microchannel plates *M* and recorded on a phosphorous screen *P* by a charge coupled device (CCD) camera outside vacuum through a viewport. The position of electrons on the screen is directly linked to the emission angle at the sample. The instrument was operated at a retarding voltage of −3 eV and with an exit aperture of 5 mm, resulting in an energy resolution of 1.2 eV and an angular resolution of 5° in the electron energy range presented here, around 480 eV. The angular resolution of only 5° is an effect of the retardation grids, and results from the high retardation ratio that had to be used at the electron energies investigated here. The acquisition time for each of the images shown here was 22.5 min.

Compensation of the angular transmission characteristics of the analyzer was achieved by normalization to the photoelectron distribution pattern of a disordered sample. A polycrystalline Fe plate had been mounted next to the Fe whisker on the same sample holder, with the two surfaces being in the same plane. An exchange between the whisker and the polycrystalline sample could thus be performed by a simple lateral displacement of the sample manipulator, keeping all other adjustments constant. A spectral background pattern of the sample, acquired at 5 eV higher kinetic energy, was subtracted first from the photoelectron distribution pattern. The result was then divided by the distribution pattern of the polycrystalline Fe sample, acquired under identical conditions, which removes the angular transmission characteristics of the display-type analyzer. Deviations from uniform transmission corrected that way were typically below 20% within 30° from normal emission direction, but amounted up to 60% at the outer edges of the images. A residual uncertainty in the photoelectron intensity of about 10% at the outer edges of the images due to possible tiny deviations in the alignment of the reference measurements cannot be excluded.

The magnetization of the sample was checked before and after the experiments by x ray magnetic circular dichroism (XMCD) in absorption, measured by the total electron yield from the sample. Quantitative analysis of the XMCD spectra revealed full remanence of the Fe magnetization over the illuminated area of the sample. Magnetization reversal was performed by a 180° azimuthal rotation of the sample. This led to a slight change in the sample surface orientation because of a small misalignment of the surface normal with respect to the azimuth rotation axis of the manipulator. The misalignment angle was determined by LEED measurements, performed within the display-type analyzer using an electron gun *E* and electrostatic deflector *D* [Fig. 1(b)], to be 1.3°, rotated about the axis of magnetization. The photoelectron distribution data are presented here after correction of

this misalignment. To avoid artifacts in the data analysis due to minute changes of the sample orientation, difference patterns were calculated only for measurements of opposite helicity but identical magnetization direction, which means identical sample position.

III. THEORY

The spin- and angle-resolved intensity of photoelectrons excited from a core state c in a solid and emitted into direction $\boldsymbol{k}=\boldsymbol{k}(k,\theta,\phi)$ with kinetic energy $E_k=\hbar^2k^2/(2m_e)$ and spin σ is given by the expression[30]

$$I_c^{\sigma}(\boldsymbol{k}) = |\langle\Psi_{\boldsymbol{k},\sigma}|H_{\omega}|\varphi_c\rangle|^2\delta(E_k-\hbar\omega-\varepsilon_c). \tag{1}$$

The δ function in Eq. (1) ensures energy conservation in the photoemission process. The operator H_{ω} is part of the perturbation operator of light which describes the absorption of a photon and depends on the polarization $\boldsymbol{u}$ and the energy $\hbar\omega$ of the incident light. The operator $H_{\omega}\propto\boldsymbol{r}\cdot\boldsymbol{u}$ is considered in the dipole approximation, where $\boldsymbol{r}$ is the electron coordinate vector.

The wave function of the core state $|\varphi_c\rangle$ with energy ε_c in Eq. (1) is treated within a one-electron theory and may be separated into a radial wave function $\phi_c(r)$ and angular and spin part $|c\rangle$. For a magnetic solid both spin–orbit interaction and exchange interaction with the spin polarized valence band (VB) have to be included in the calculation of the core state. In a one-electron model these contributions are given by the interaction Hamiltonian[31]

$$H_{int} = \lambda\boldsymbol{l}\cdot\boldsymbol{s} + \zeta s_z. \tag{2}$$

The first term in Eq. (2) is the spin–orbit coupling with strength λ. The second term in Eq. (2) represents the exchange interaction between core state and VB by means of a homogeneous spin field along the z axis, which is chosen along the direction of magnetization $\boldsymbol{M}$. It is reasonable to use the eigenfunctions of the spin–orbit Hamiltonian $H_{so}=\lambda\boldsymbol{l}\cdot\boldsymbol{s}$ as basis functions of $|c\rangle$,

$$|jl\mu\rangle = \sum_{m,\sigma} C^{j\mu}_{lm,(1/2)\sigma}|lm\sigma\rangle, \tag{3}$$

in which the Clebsch-Gordan coefficients $C^{j\mu}_{lm,(1/2)\sigma}$ (Ref. 32) depend on the quantum numbers of the total momentum $j=l\pm1/2$ and $\mu=-j,-j+1,\ldots,+j$, and on the quantum numbers of the angular momentum l and $m=-l,-l+1,\ldots,+l$, respectively. The exchange interaction $H_{ex}=\zeta s_z$ leads in general to a mixing of $j^+=l+1/2$ and $j^-=l-1/2$ states having the same value of μ, which is still a good quantum number. In this case the spin and angular part $|c\rangle=|\psi_{\nu}(\mu)\rangle$ is written as a linear combination of states $|j^{\pm}l\mu\rangle$:

$$|\psi_{\nu}(\mu)\rangle = c^+_{\nu\mu}(\zeta)|j^+l\mu\rangle + c^-_{\nu\mu}(\zeta)|j^-l\mu\rangle \quad (\nu=1,2). \tag{4}$$

The mixing coefficients $c^{\pm}_{\nu\mu}$ and the related energy eigenvalues $\varepsilon_{\nu}(\mu)$ are estimated by solving the eigenvalue problem for the interaction Hamiltonian (2). For pure $j=3/2$ ($j=1/2$) the mixing coefficients in Eq. (4) are $c^+_{\nu\mu}=1$ ($c^-_{\nu\mu}=0$) and $c^-_{\nu\mu}=1$ ($c^+_{\nu\mu}=0$) for all values ($\nu\mu$).

By substituting Eq. (3) into Eq. (4), the function $|\psi_{\nu}(\mu)\rangle$ can be expressed in terms of $|lm\sigma\rangle$, however, the coefficients of this linear combination

$$A^{m\sigma}_{\nu}(\mu) = c^+_{\nu\mu}(\zeta)C^{j^+\mu}_{lm,(1/2)\sigma} + c^-_{\nu\mu}(\zeta)C^{j^-\mu}_{lm,(1/2)\sigma} \tag{5}$$

have lost the symmetry properties of the Clebsch-Gordan coefficients, in particular for transformation $\{m,\sigma\}\rightarrow\{-m,-\sigma\}$. The model Hamiltonian (2) has been discussed recently for different systems, where λ and ζ have been considered as parameters to explain experimental results of core-level photoemission.[33]

The final state of photoelectrons $|\Psi_{\boldsymbol{k},\sigma}\rangle$ in Eq. (1) is calculated within a multiple-scattering cluster (MSC) model.[34] The scattering properties of the system are described by scattering phase shifts $\delta_{l\sigma}$ calculated within a muffin-tin model for each kind of atom. The spin dependence of the scattering phase shifts appears in magnetic systems due to the spin-dependent effective one-electron potential.

In the angular momentum representation $[L\equiv(l,m)]$ the spin- and angle-resolved intensity (1) of photoelectrons may be written in the form

$$I^{\sigma}_{\nu\mu}(\boldsymbol{k}) \propto \sum_{\boldsymbol{R}_0}\left|\sum_{L} B^{\boldsymbol{R}_0}_{L\sigma}(\boldsymbol{k})M^{\boldsymbol{R}_0}_{L\sigma,\nu\mu}(E_k,\boldsymbol{u})\right|^2, \tag{6}$$

where both spin–orbit and exchange interaction in the initial state in a magnetic sample have been taken into account. The sum about $\boldsymbol{R}_0$ in Eq. (6) runs over all contributions of different emitters at sites $\boldsymbol{R}_0$, where the photon is absorbed creating a hole state $|\varphi_c\rangle$. The scattering path operator $B_{L\sigma}$ contains the direct, single-scattering, and multiple-scattering contributions of the photoelectron.[35,36] Which L values will contribute to the intensity (6) is determined by the dipole transition matrix element

$$M_{L\sigma,\nu\mu}(E_k,\boldsymbol{u}) = R_{l\sigma}(E_k)\langle L\sigma|\hat{\boldsymbol{r}}\cdot\boldsymbol{u}|\psi_{\nu}(\mu)\rangle, \tag{7}$$

containing the angular and spin part of the final state $|L\sigma\rangle$ and the initial core state $|\psi_{\nu}(\mu)\rangle$. The radial part of the dipole matrix element in Eq. (7) is given by $R_{l\sigma}=\exp(i\delta_{l\sigma})\langle\phi_{l\sigma}|r|\phi_c\rangle$.

In the calculation of spin-resolved core-level spectra as a function of energy E for fixed emission direction $\boldsymbol{k}$, the single ($\nu\mu$) contributions of the intensity (6) at position $\varepsilon_{\nu}(\mu)$ were additionally broadened by Gaussian or Lorentzian broadening functions $P_{\nu\mu}(E)$:

$$I^{\sigma}(E;\boldsymbol{k}) = \sum_{(\nu\mu)} I^{\sigma}_{\nu\mu}(\boldsymbol{k})P_{\nu\mu}(E-\varepsilon_{\nu}(\mu)). \tag{8}$$

In the limit $\lambda\gg\zeta$, which is closely realized for a $2p$ core level, the sublevels j^+ and j^- are shifted energetically by $+\lambda/2$ and $-\lambda$ with respect to the one-electron energy ε_c. This leads to a spin–orbit splitting Δ_{so} of 1.5λ. The exchange splitting Δ_{ex} between adjacent sublevels μ amounts then to $\zeta/3$. Reversing the direction of magnetization ($\zeta\rightarrow-\zeta$) merely interchanges the energetic positions of sublevels μ and $-\mu$ for the energetically well-separated $j^{\pm}$ sublevels. This leads to the well-known plus–minus features in the difference spectrum of core-level spectra.

The circular dichroism in the angular distribution (CDAD) of photoelectrons is determined by the difference between the intensities of photoelectrons excited by circularly polarized light of positive and negative helicity,[37]

$$\mathrm{CDAD}(\theta,\phi) = I(\theta,\phi;\boldsymbol{u}^+) - I(\theta,\phi;\boldsymbol{u}^-), \tag{9}$$

where $\boldsymbol{u}^+$ and $\boldsymbol{u}^-$ mark the positive and negative helicity of light, respectively.

The CDAD of photoelectrons excited from deep core levels in single crystals is caused mainly by photoelectron diffraction effects.[38,39] In the case of electron energies of several hundred eV, PED is dominated by forward scattering contributions which are related to the local geometric structure around the emitter. The observed CDAD can be understood by a merely azimuthal shift ("peak rotation") $\Delta\phi$ of forward scattering peaks in the PED pattern, which is opposite for circularly polarized light of positive and negative helicity, respectively. A simple formula for this shift

$$\Delta\phi = \frac{m_0}{kR\sin^2\theta} \tag{10}$$

was derived first from wave mechanics[21] and later from PED theory.[40,41] The quantum number m_0 in Eq. (10) is just the opposite for light of positive and negative helicity, and follows from the main contribution of the dipole transition (7). Recently, an improved expression has been found[22,42] where all allowed (l,m) values have been taken into account. In this case m_0 in Eq. (10) has to be replaced by $m^*(\theta,cr)$, where $cr = R_{l_c-1}/R_{l_c+1}$ is the ratio of the complex radial matrix elements of the considered transition.

In case of magnetic systems the degeneracy of the core level is lifted due to exchange interaction, and the scattering phase shifts for spin-up and spin-down electrons are different. Apart from the azimuthal shift of forward scattering peaks, a difference between intensities $I(\Delta\phi;\boldsymbol{u}^{\pm})$ arises which depends on the local magnetic order around the emitter. Analysis of the related symmetry breaking in the CDAD of photoelectrons can be used to reveal the magnetic information contained in the photoelectron diffraction patterns.

To compare with experimental results, we calculated the intensity $I^{\sigma}_{\nu\mu}(\boldsymbol{k})$ [Eq. (6)] for the excitation of Fe $2p_{3/2}$ photoelectrons in Fe(001) upon helicity reversal and in dependence on magnetization direction $\boldsymbol{M}^+$ and $\boldsymbol{M}^-$. Multiple-scattering calculations up to fifth order have been done for an iron cluster of 250 atoms with Fe emitters in five layers. In the considered energy region ($E_k \approx 480$ eV) a possible small relaxation at the iron surface has been neglected. The inelastic damping has been taken into account by an imaginary potential $V_{0i} \approx 10$ eV. The spin dependent scattering phase shifts $\delta_{l\sigma}$ followed from a calculation with magnetic moments 2.15 μ_B/atom. All calculated intensities were normalized to the calculated unscattered contribution to the photoelectron intensity in order to match the experimental normalization by the photoelectron angular distribution of a polycrystalline sample (cf. Sec. II). An angular averaging of 2° has been applied to the calculated data in order to smoothen out narrow spikelike structures that would not be observable in experiment. This angular averaging was chosen to be still significantly smaller than the experimental angular resolution so that the theoretical angular distribution patterns yield more detailed information about the influence of magnetic scattering events than the experimental ones.

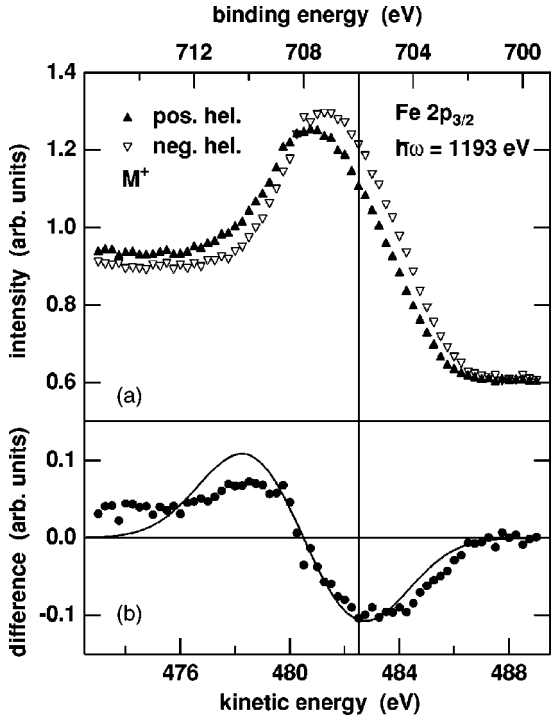

FIG. 2. (a) Fe $2p_{3/2}$ core-level spectra for excitation with circular polarization of positive (closed symbols) and negative helicity (open symbols) for 1193 eV photon energy. (b) Closed circles: Difference spectrum of the two curves shown in panel (a). Line: Calculated difference spectrum, scaled by a factor of 0.5. Note that also the vertical scale is different compared to panel (a) (factor of 2). The vertical line marks the kinetic energy of 482.5 eV, at which photoelectron diffraction patterns have been acquired.

IV. RESULTS

In Fig. 2(a) two Fe $2p_{3/2}$ core-level spectra are reported as a function of photoelectron kinetic energy. Spectra for circularly polarized light of positive and negative helicity are represented by closed and open symbols, respectively. The photon energy is 1193 eV, and the magnetization $\boldsymbol{M}^+$ is along the $\langle 100\rangle$ direction of Fe(001) ($\phi = 0°$). The spectra have been obtained by averaging the photoelectron intensity over the entire detector fluorescent screen without compensation of the angular transmission characteristics of the spectrometer. This results in an angle-averaged electron energy spectrum, with an enhanced weighting of the near-normal emission directions.

The Fe $2p_{3/2}$ intensity line shapes in Fig. 2(a) appear slightly asymmetric, with the higher binding energy side of the lines enlarged, in good agreement with a Doniach-Šunjić type line shape.[44] The experimental difference spectrum, shown by closed circles in Fig. 2(b), is, as expected, positive for energies $E < 481$ eV and negative for $E > 481$ eV.[3] Although the energy scan includes only the Fe $2p_{3/2}$ peak and

not the $2p_{1/2}$ peak, and does thus not allow one to double check the mutual normalization of the two spectra acquired for opposite light helicity, the corresponding uncertainty of the zero line of Fig. 2(b) is less than 0.02 y (difference) axis units.

The observed plus–minus feature in Fig. 2(b) is well known and has been discussed in detail in the literature.[3,5,15,16] If the helicity of light is reversed, the energetic positions of minority and majority electrons in the emission spectrum are interchanged. To explain the measured Fe $2p_{3/2}$ core-level spectra of Fig. 2 (after subtraction of a constant background), the intensity $I(E;\boldsymbol{k})$ has been calculated from Eq. (8), added for both σ and for all values of μ corresponding to $j=3/2$, and broadened by a Gaussian of width σ_0. The best agreement has been found for $\Delta_{ex}=1.5$ eV and $\sigma_0=1.1$ eV. The resulting energy difference between adjacent μ-core levels of $\Delta_{ex}/3=0.5$ eV is comparable to other commonly used values.[9,33]

The corresponding calculated difference spectrum for normal emission is plotted as a line in Fig. 2(b), scaled by a factor of 0.5 after normalization to the experimental photoemission peak height. The agreement between the theoretical and the experimental difference spectra is quite good, considering the not very precisely known angular weighting of the photoelectrons collected in the experimental spectra, while the calculated spectrum corresponds exactly to the normal emission direction. The vertical line marks the kinetic energy of 482.5 eV, at which the photoelectron diffraction patterns presented in the following have been obtained. A strong magnetic effect is expected at that energy.

In Fig. 3 experimental two-dimensional photoelectron diffraction patterns of Fe $2p_{3/2}$ photoelectrons are shown for all four combinations of magnetization direction and light helicity. The top row [Figs. 3(a) and 3(c)] displays the patterns for magnetization $\boldsymbol{M}^+$, the bottom row [Figs. 3(b) and 3(d)] for magnetization $\boldsymbol{M}^-$. The patterns on the left-hand side [Figs. 3(a) and 3(b)] have been acquired for positive helicity, the patterns on the right-hand side [Figs. 3(c) and 3(d)] for negative helicity.

The main contribution to the intensity of photoelectrons is expected along forward scattering directions in the Fe(001) whisker. A strong CDAD is directly visible as a shift of these intense forward scattering spots towards the lower part of the displayed patterns when changing the helicity from positive to negative. This can be interpreted as a "peak rotation" of the forward scattering spots around the direction of light incidence, which in the representation of Fig. 3 is at the very left of the plot, at $\theta=45°$, $\phi=180°$, cf. Fig. 1(a). For a nonmagnetic surface we would expect the fulfillment of the symmetry relation along the mirror plane in the experimental geometry ($\phi_0=0°$ and $\phi_0=180°$)

$$I(\phi_0+\phi;\boldsymbol{u}^+)=I(\phi_0-\phi;\boldsymbol{u}^-). \tag{11}$$

This means that for nonmagnetic samples the upper hemisphere of the diffraction pattern acquired with light of positive helicity should be mirror-identical to the lower hemisphere of the diffraction pattern acquired with negative helicity, and vice versa. This symmetry relation is broken in the presence of magnetism.

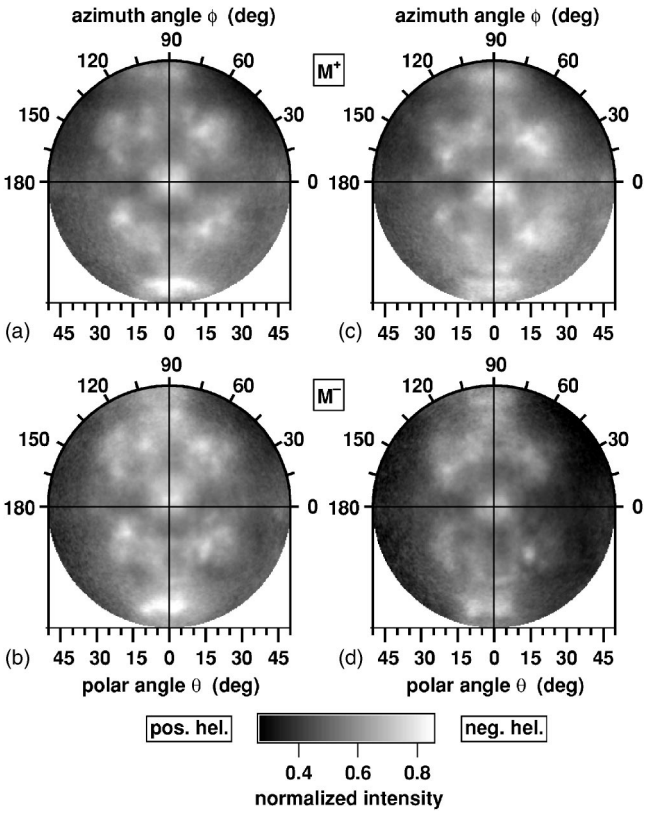

FIG. 3. Experimental two-dimensional photoelectron diffraction patterns of Fe $2p_{3/2}$ photoelectrons at 482.5 eV electron energy. (a) Positive helicity and $\boldsymbol{M}^+$, (b) positive helicity and $\boldsymbol{M}^-$, (c) negative helicity and $\boldsymbol{M}^+$, and (d) negative helicity and $\boldsymbol{M}^-$.

The strong CDAD, caused by PED effects of the excited photoelectrons, can be well described within the multiple-scattering cluster model.[40,43] Theoretical results are shown in Fig. 4. Panels (a)–(d) correspond to the four experimental photoelectron distribution patterns for the four combinations of light helicity and magnetization direction (upper row is for magnetization $\boldsymbol{M}^+$, left column is for positive helicity).

As in the experiment, the CDAD is most prominent in a vertical shift of the main features, which move down when switching from positive to negative helicity (best seen at the central spot in Fig. 4). The breaking of the symmetry relation (11) is most evident as a different overall intensity. Note that in the presence of a sample magnetization along the horizontal direction of the patterns, symmetry requires the upper hemisphere of panel (a) to equal the mirror image of the lower hemisphere of panel (d), and vice versa. The same holds for panels (b) and (c).

The main features in the experimental pattern are well described by the MSC calculations. In Fig. 5 a comparison between the experimental (left) and the theoretical (right) CDAD of Fe $2p_{3/2}$ photoelectrons for both magnetizations is shown. According to Eq. (9) it is defined as the difference between the photoelectron intensity distribution patterns obtained for positive and for negative helicity. The upper panels (a) and (c) correspond to magnetization $\boldsymbol{M}^+$, the lower panels (b) and (d) to magnetization $\boldsymbol{M}^-$. The main difference between the two magnetizations is the overall intensity in the

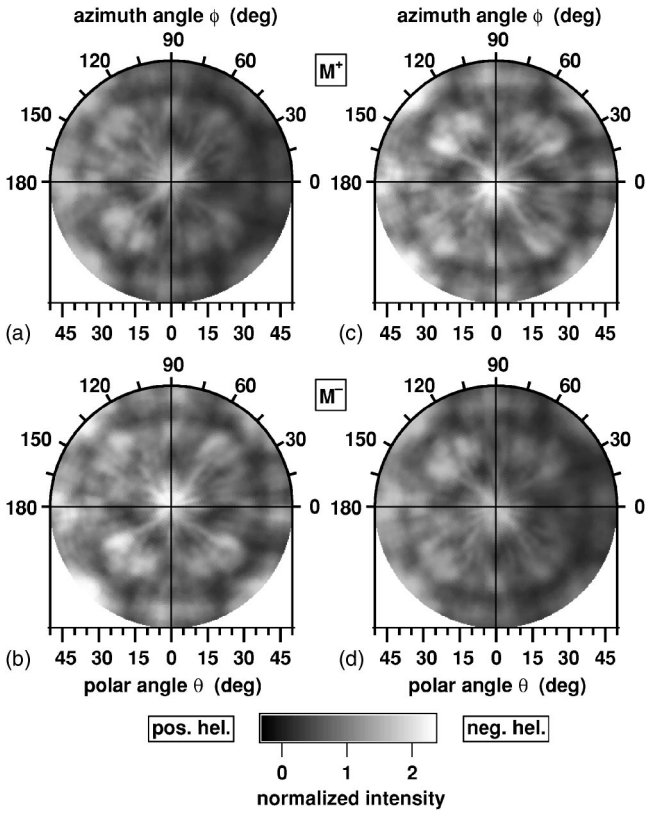

FIG. 4. Calculated two-dimensional photoelectron diffraction patterns of Fe $2p_{3/2}$ photoelectrons at 482.5 eV electron energy. (a) Positive helicity and $\boldsymbol{M}^+$, (b) positive helicity and $\boldsymbol{M}^-$, (c) negative helicity and $\boldsymbol{M}^+$, and (d) negative helicity and $\boldsymbol{M}^-$.

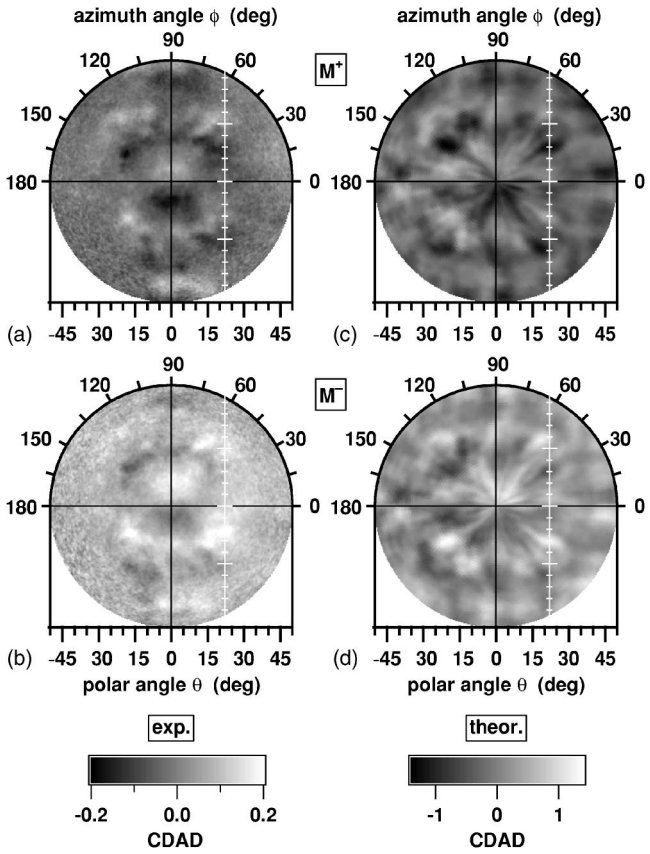

FIG. 5. Comparison between experimental and calculated two-dimensional angular CDAD patterns. (a) Experimental CDAD for magnetization $\boldsymbol{M}^+$, (b) experimental CDAD for magnetization $\boldsymbol{M}^-$, (c) theoretical CDAD for magnetization $\boldsymbol{M}^+$, and (d) theoretical CDAD for magnetization $\boldsymbol{M}^-$. Vertical white lines in (a) and (c) indicate positions at which vertical linescans presented in Fig. 6 have been taken.

CDAD patterns, which is due to exchange interaction. This is quite well reproduced in the calculation. Nearly all of the features of the experimental CDAD patterns can be correlated to features in the calculated patterns. Due to the experimental angular resolution of 5°, the main structures seem a bit more smeared out in the experimental CDAD images compared to the theoretical ones. The most intense features in the calculated CDAD appear along forward scattering directions, the position of which is different by a few degrees for each light helicity (forward-scattering peak rotation, cf. Refs. 21, 22, 38, 40, 41, and 45). Within a simple single-scattering calculation these contributions would be strongly overestimated. Due to multiple scattering along chains of atoms these contributions are reduced but give nevertheless a sharp peak in the calculated CDAD.

For a more detailed comparison between experiment and theory linescans of the CDAD angular distribution patterns are displayed in Fig. 6. The linescans have been taken along vertical lines indicated in Figs. 5(a) and 5(c) by white lines. To simplify the discussion of the features, the x axis of Fig. 6 has been numbered equidistantly from −1 to +1 and called "linescan position" in the following, where −1 corresponds to the lower end of the white lines shown in Fig. 5. Minor ticks indicate increments of 0.1. Figure 6(a) shows linescans of the experimental CDAD, and Fig. 6(b) linescans of the theoretical CDAD. Solid and dotted lines correspond to magnetization $\boldsymbol{M}^+$ and $\boldsymbol{M}^-$, respectively.

The overall structure and main features of the experimental linescans are well reproduced by the calculation. The symmetry breaking due to the presence of magnetization is evident by the different offset of the curves for positive and negative magnetization along the vertical, but also from characteristic differences in the details of both the experimental and theoretical curves. The positive peak around −0.3 linescan position, for example, is stronger for magnetization $\boldsymbol{M}^-$ than for $\boldsymbol{M}^+$, while for symmetry reasons the corresponding negative peak at +0.3 linescan position is stronger for magnetization $\boldsymbol{M}^+$ than for $\boldsymbol{M}^-$. In addition, the peak positions of these extrema along the direction of the linescan are different. In the experiment, these two peaks are shifted to the left for magnetization $\boldsymbol{M}^+$ compared to magnetization $\boldsymbol{M}^-$. The same effect is also present in the calculation, but less pronounced. The peaks in the theoretical linescans [Fig. 6(b)] are much larger than the corresponding experimental peaks [Fig. 6(a); note the different vertical scales in panels (a) and (b)]. The main reason could be the different angular averaging in experiment and theory, which can strongly influence the amplitudes of structures in CDAD difference images. Background contributions in the experimental data which could not be subtracted, such as scattering at impuri-

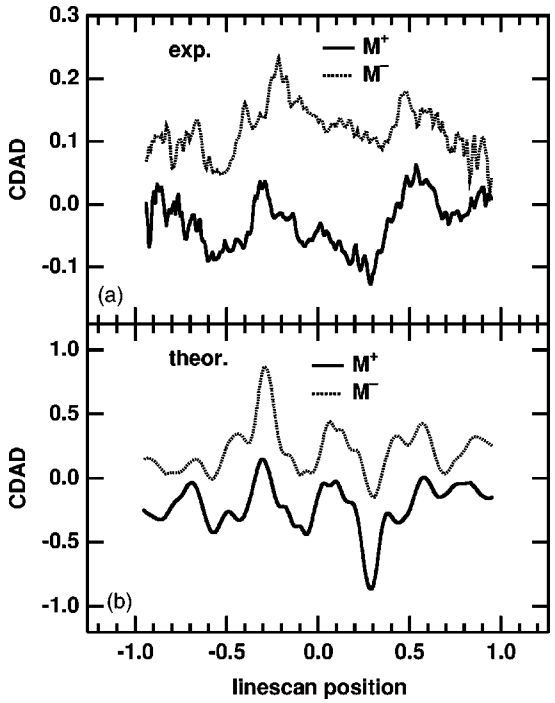

FIG. 6. Experimental (a) and theoretical (b) linescans of the CDAD angular distribution patterns shown in Fig. 5 for magnetization $\boldsymbol{M}^+$ (solid lines) and $\boldsymbol{M}^-$ (dotted lines).

ties or surface contaminants, or structural imperfections at the surface, may also influence the absolute value of the CDAD to a minor extent, as well as a possible small residual overestimation of the forward focusing photoelectron intensity resulting from the cutoff after fifth order of multiple electron scattering events in the calculation. The experimental curves are not fully centrosymmetric about zero, but exhibit a shift of about 5% towards positive values. This has to be attributed to experimental artifacts such as slight misadjustings of the sample to detector distance, which can influence the photoelectron intensity. It should be noted that this artifactual shift is smaller than the vertical offset of the curves as a consequence of the magnetism-induced symmetry breaking. It may, however, hamper the quantitative comparison of the size of the symmetry breaking between experiment and theory.

The shape of the theoretical and experimental linescans differs around zero linescan position in Fig. 6. Whereas in the theoretical data a strong maximum is observed for both magnetizations $\boldsymbol{M}^+$ and $\boldsymbol{M}^-$, there is only a small structure in the experimental data. At the moment we are not able to explain these small differences between experiment and calculation. The slightly different peak positions may be due to small inaccuracies in the experimental sample adjustment for the two magnetization directions. Overall, however, the agreement is quite good, and even fine details of the symmetry breaking by the presence of a macroscopic magnetization are well described by the calculation.

Summarizing our findings, we observed that the "peak rotation", which is present also in the CDAD of nonmagnetic samples, occurs in the same way for both magnetization directions $\boldsymbol{M}^{\pm}$, and constitutes the major effect leading to different angular diffraction spot positions when changing the light helicity. From that peak rotation, conclusions about the sample structure may be drawn already without theoretical calculations provided certain assumptions about the quantum numbers of the contributing transitions can be made.[21,22] While the most prominent effect of the symmetry breaking by the sample magnetization is a different overall intensity of the photoelectron diffraction patterns, which show a higher intensity for $\boldsymbol{M}^-$ compared to $\boldsymbol{M}^+$ for the considered higher kinetic energy side of the Fe $2p_{3/2}$ peak, it is also manifest in finer details of the photoelectron angular distribution patterns. A shift of angular spot positions and different relative peak heights in the CDAD for opposite sample magnetization are two examples. Both are well reproduced by the theoretical calculation. The magnetism-induced symmetry breaking in the angular distribution patterns of photoelectrons may thus provide the basis for the investigation of the local magnetic structure in more complex samples.

V. CONCLUSIONS

The presented theoretical and experimental results clearly show how the CDAD of photoelectrons is influenced by the magnetic properties of the sample. The strong CDAD at a solid surface is caused mainly by scattering of the excited photoelectrons. Because of the magnetic moments of the Fe atoms, the scattering of spin-up and spin-down electrons is different. The magnetism-induced symmetry breaking observed in the experiment for Fe $2p$ photoelectrons in Fe(001) is of the order of 10%, hence large enough to be used for experimental studies of magnetic surfaces. Recording full two-dimensional photoelectron diffraction patterns and forming the related magnetism-induced symmetry breaking constitutes a new direct method to investigate both the local magnetic and geometric order of magnetic samples. The improved multiple-scattering cluster model of photoelectron diffraction provides an excellent description of the experimentally observed CDAD and magnetism-induced symmetry breaking in photoelectron diffraction patterns of Fe $2p_{3/2}$ photoelectrons in Fe(001). Experimental investigations of photoelectron scattering effects on the CDAD, backed with multiple-scattering cluster calculations, bear the potential to study also systems with complex spin structures such as antiferromagnets and ferrimagnets, or to investigate ultrathin films with inhomogeneous vertical magnetization properties.

ACKNOWLEDGMENTS

We are grateful for financial support by BMBF (No. 05 SL8EF1 9), JSPS, and DFG (No. Ki 358/3-2 and No. 446 JAP-113/179/0). We would like to thank B. Zada for assistance in shipping of equipment and for dealing with custom's procedures. The experiments were performed at SPring-8 with the approval and financial support of JASRI (No. 2000A0051-NS-np). Our special thanks is for the SPring-8 staff, in particular Y. Saitoh, for generous help during the beamtime.

*Present address: Freie Universität Berlin, Institut für Experimentalphysik, Arnimallee 14, D-14195 Berlin, Germany.
†Present address: Hiroshima Synchrotron Radiation Center, 2-313 Kagamiyama, Higashi-Hiroshima 739-8526, Japan.
‡Present address: Faculty of Science, National University of Singapore, Department of Physics, 2 Science Drive 3, Singapore 117542.
§Present address: INFM, Unità Roma Tre, Via della Vasca Navale 84, I-00146 Roma, Italy.

[1] H. Daimon, Phys. Rev. Lett. **86**, 2034 (2001); H. Daimon, R. Ynzunza, J. Palomares, H. Takabi, and C. S. Fadley, Surf. Sci. **408**, 260 (1998); G. C. Gazzadi, P. Luches, A. di Bona, L. Marassi, L. Pasquadi, S. Valeri, and S. Nannarone, Phys. Rev. B **61**, 2246 (2000); T. Greber, J. Wider, E. Wetli, and J. Osterwalder, Phys. Rev. Lett. **81**, 1654 (1998); E. Hüger and K. Osuch, Europhys. Lett. **62**, 278 (2003); M. G. Martin, E. Foy, F. Chevrier, G. Krill, and M. C. Asensio, Surf. Sci. **433-435**, 88 (1999); K. Reuter, J. Bernhardt, H. Wedler, J. Schardt, U. Starke, and K. Heinz, Phys. Rev. Lett. **79**, 4818 (1997); A. Theobald, S. Bao, V. Fernandez, K.-M. Schindler, O. Schaff, V. Fritzsche, A. M. Bradshaw, N. Booth, and D. P. Woodruff, Surf. Sci. **385**, 107 (1997); E. D. Tober, R. X. Ynzunza, F. J. Palomares, Z. Wang, Z. Hussain, M. A. Van Hove, and C. S. Fadley, Phys. Rev. Lett. **79**, 2085 (1997).

[2] W. Kuch, A. Dittschar, K. Meinel, M. Zharnikov, C. M. Schneider, J. Kirschner, J. Henk, and R. Feder, Phys. Rev. B **53**, 11621 (1996); D. Venus, *ibid.* **56**, 2661 (1997).

[3] L. Baumgarten, C. M. Schneider, H. Petersen, F. Schäfers, and J. Kirschner, Phys. Rev. Lett. **65**, 492 (1990); F. U. Hillebrecht, Ch. Roth, H. B. Rose, M. Finazzi, and L. Braicovich, Phys. Rev. B **51**, 9333 (1995); J. G. Tobin, G. D. Waddill, D. P. Pappas, E. Tamura, P. A. Sterne, X. Guo, and S. Y. Tong, J. Vac. Sci. Technol. A **13**, 1534 (1995).

[4] J. Bansmann, L. Lu, K. H. Meiwes-Broer, T. Schlathölter, and J. Braun, Phys. Rev. B **60**, 13860 (1999).

[5] Ch. Roth, F. U. Hillebrecht, H. B. Rose, and E. Kisker, Phys. Rev. Lett. **70**, 3479 (1993); Ch. Roth, H. B. Rose, F. U. Hillebrecht, and E. Kisker, Solid State Commun. **86**, 647 (1993); F. Sirotti and G. Rossi, Phys. Rev. B **49**, 15682 (1994); G. Rossi, G. Panaccione, F. Sirotti, and N. A. Cherepkov, *ibid.* **55**, 11483 (1997); G. Panaccione, F. Sirotti, and G. Rossi, Solid State Commun. **113**, 373 (2000); W. Kuch, M.-T. Lin, W. Steinhögl, C. M. Schneider, D. Venus, and J. Kirschner, Phys. Rev. B **51**, 609 (1995).

[6] H. B. Rose, Ch. Roth, F. U. Hillebrecht, and E. Kisker, Solid State Commun. **91**, 129 (1994); D. Venus, W. Kuch, M.-T. Lin, C. M. Schneider, H. Ebert, and J. Kirschner, Phys. Rev. B **55**, 2594 (1997); A. Rampe, G. Güntherodt, D. Hartmann, J. Henk, T. Scheunemann, and R. Feder, *ibid.* **57**, 14370 (1998).

[7] M. Getzlaff, Ch. Ostertag, G. H. Fecher, N. A. Cherepkov, and G. Schönhense, Phys. Rev. Lett. **73**, 3030 (1994).

[8] F. U. Hillebrecht and W.-D. Herberg, Z. Phys. B: Condens. Matter **93**, 299 (1994); A. Fanelsa, R. Schellenberg, F. U. Hillebrecht, E. Kisker, J. G. Menchero, A. P. Kaduwela, C. S. Fadley, and M. A. van Hove, Phys. Rev. B **54**, 17962 (1996).

[9] R. Schellenberg, E. Kisker, M. Faust, A. Fanelsa, and F. U. Hillebrecht, Phys. Rev. B **58**, 81 (1998); R. Schellenberg, E. Kisker, A. Fanelsa, F. U. Hillebrecht, J. G. Menchero, A. P. Kaduwela, C. S. Fadley, and M. A. Van Hove, *ibid.* **57**, 14310 (1998).

[10] X. Gao, M. Salvietti, W. Kuch, C. M. Schneider, and J. Kirschner, Phys. Rev. B **58**, 15426 (1998).

[11] X. Gao, M. Salvietti, W. Kuch, C. M. Schneider, and J. Kirschner, J. Electron Spectrosc. Relat. Phenom. **113**, 137 (2001).

[12] C. M. Schneider, U. Pracht, W. Kuch, A. Chassé, and J. Kirschner, Phys. Rev. B **54**, R15618 (1996).

[13] W. Kuch and C. M. Schneider, Rep. Prog. Phys. **64**, 147 (2001).

[14] H. Ebert, J. Phys.: Condens. Matter **1**, 9111 (1989); H. Ebert, L. Baumgarten, C. M. Schneider, and J. Kirschner, Phys. Rev. B **44**, 4406 (1991).

[15] B. T. Thole and G. van der Laan, Phys. Rev. Lett. **67**, 3306 (1991); Phys. Rev. B **44**, 12424 (1991); G. van der Laan, Phys. Rev. Lett. **66**, 2527 (1991).

[16] E. Tamura, G. D. Waddill, J. G. Tobin, and P. A. Sterne, Phys. Rev. Lett. **73**, 1533 (1994).

[17] G. D. Waddill, J. G. Tobin, X. Guo, and S. Y. Tong, Phys. Rev. B **50**, 6774 (1994).

[18] B. Sinković, B. Hermsmeier, and C. S. Fadley, Phys. Rev. Lett. **55**, 1227 (1985); E. D. Tober, F. J. Palomares, R. X. Ynzunza, R. Denecke, J. Morais, Z. Wang, G. Bino, J. Liesegang, Z. Hussain, and C. S. Fadley, *ibid.* **81**, 2360 (1998); Yu. Kucherenko and P. Rennert, J. Phys.: Condens. Matter **9**, 5003 (1997).

[19] F. U. Hillebrecht, H. B. Rose, T. Kinoshita, Y. U. Idzerda, G. van der Laan, R. Denecke, and L. Ley, Phys. Rev. Lett. **75**, 2883 (1995).

[20] S. Y. Tong, X. Guo, J. G. Tobin, and G. D. Waddill, Phys. Rev. B **54**, 15356 (1996).

[21] H. Daimon, T. Nakatani, S. Imada, S. Suga, Y. Kagoshima, and T. Miyahara, Jpn. J. Appl. Phys., Part 2 **32**, L1480 (1993).

[22] H. Daimon, S. Imada, and S. Suga, Surf. Sci. **471**, 143 (2001).

[23] A. Chassé, L. Niebergall, and P. Rennert, J. Electron Spectrosc. Relat. Phenom. **101-103**, 335 (1999).

[24] P. Rennert, W. Mück, and A. Chassé, Phys. Rev. B **53**, 14262 (1997); Surf. Sci. **357-358**, 260 (1996).

[25] P. Rennert, A. Chassé, and L. Niebergall, Surf. Sci. **454-456**, 870 (2000).

[26] J. B. Pendry, Surf. Sci. **57**, 697 (1976); C. H. Li, A. R. Lubinsky, and S. Y. Tong, Phys. Rev. B **17**, 3128 (1978).

[27] B. Heinrich and J. F. Cochran, Adv. Phys. **42**, 523 (1993).

[28] Y. Saitoh, T. Nakatani, T. Matsushita, T. Miyahara, M. Fujisawa, K. Soda, T. Muro, S. Ueda, H. Harada, A. Sekiyama, S. Imada, H. Daimon, and S. Suga, J. Synchrotron Radiat. **5**, 542 (1998).

[29] M. Kotsugi, Y. Miyatake, K. Enomoto, K. Fukumoto, A. Kobayashi, T. Nakatani, Y. Saitoh, T. Matsushita, S. Imada, T. Furuhata, S. Suga, K. Soda, M. Jinno, T. Hirano, K. Hattori, and H. Daimon, Nucl. Instrum. Methods Phys. Res. A **467-468**, 1493 (2001).

[30] A. Liebsch, Phys. Rev. B **13**, 544 (1976).

[31] H. Ebert, J. Phys.: Condens. Matter **1**, 9111 (1989); G. van der Laan, Phys. Rev. B **51**, 240 (1995).

[32] A. Messiah, *Quantum Mechanics* (North-Holland, Amsterdam, 1962).

[33] J. G. Menchero, Phys. Rev. B **57**, 993 (1998); Yu. Kucherenko, B. Sinkovic, E. Shekel, P. Rennert, and S. Hulbert, *ibid.* **62**, 5733 (2000); J. Henk, A. M. N. Niklasson, and B. Johansson, *ibid.* **59**, 13986 (1999).

[34] P. Rennert and A. Chassé, Exp. Tech. Phys. (Berlin) **35**, 27 (1987); A. Chassé and P. Rennert, Phys. Status Solidi B **138**, 53 (1986).

[35] O. Speder, P. Rennert, and A. Chassé, Surf. Sci. **331-333**, 1383 (1995).

[36] A. Chassé, J. Phys.: Condens. Matter **11**, 6475 (1999), and references therein.
[37] G. Schönhense, Phys. Scr., T **T31**, 255 (1990); J. Bansmann, Ch. Ostertag, M. Getzlaff, G. Schönhense, N. A. Cherepkov, V. V. Kuznetsov, and A. A. Pavlychev, Z. Phys. D: At., Mol. Clusters **33**, 257 (1995), and references therein.
[38] H. Daimon, T. Nakatani, S. Imada, and S. Suga, Rev. Sci. Instrum. **66**, 1510 (1995); J. Electron Spectrosc. Relat. Phenom. **76**, 55 (1995).
[39] C. S. Fadley, M. A. Van Hove, Z. Hussain, and A. P. Kaduwela, J. Electron Spectrosc. Relat. Phenom. **75**, 273 (1995), and references therein.
[40] A. Chassé and P. Rennert, J. Electron Spectrosc. Relat. Phenom. **87**, 91 (1997).
[41] A. Chassé and P. Rennert, Phys. Rev. B **55**, 4120 (1997).
[42] P. Rennert, J. Electron Spectrosc. Relat. Phenom. **119**, 1 (2001).
[43] P. Rennert, A. Chassé, T. Nakatani, K. Nakatsuji, H. Daimon, and S. Suga, J. Phys. Soc. Jpn. **66**, 396 (1997).
[44] S. Doniach and M. Šunjić, J. Phys. C **3**, 285 (1970).
[45] H. Daimon, R. X. Ynzunza, F. J. Palomares, E. D. Tober, Z. X. Wang, A. P. Kaduwela, M. A. Van Hove, and C. S. Fadley, Phys. Rev. B **58**, 9662 (1998).